Quantifying Retinal Pigment Epithelium Dysmorphia and Loss of Histologic Autofluorescence in Age-Related Macular Degeneration

J. Alan Gambril,[1] Kenneth R. Sloan,[1] Thomas A. Swain,[1] Carrie Huisingh,[1] Anna V. Zarubina,[1] Jeffrey D. Messinger,[1] Thomas Ach,[2] and Christine A. Curcio[1]

[1]Department of Ophthalmology and Visual Sciences, University of Alabama at Birmingham School of Medicine, Birmingham, Alabama, United States
[2]Department of Ophthalmology, University Hospital Würzburg, Würzburg, Germany

Correspondence: Christine A. Curcio, Department of Ophthalmology and Visual Sciences, EyeSight Foundation of Alabama Vision Research Laboratories, 1670 University Boulevard, Room 360, University of Alabama at Birmingham School of Medicine, Birmingham, AL 35294-0099, USA; christinecurcio@uabmc.edu.

TA and CAC are joint senior authors.

Submitted: February 22, 2019
Accepted: May 4, 2019

Citation: Gambril JA, Sloan KR, Swain TA, et al. Quantifying retinal pigment epithelium dysmorphia and loss of histologic autofluorescence in age-related macular degeneration. *Invest Ophthalmol Vis Sci*. 2019;60:2481–2493. https://doi.org/10.1167/iovs.19-26949

Purpose. Lipofuscin and melanolipofuscin organelles in retinal pigment epithelium (RPE) cells are signal sources for clinical fundus autofluorescence (AF). To elucidate the subcellular basis of AF imaging, we identified, characterized, and quantified the frequency of RPE morphology and AF phenotypes in donor eyes with age-related macular degeneration (AMD).

Methods. In 25 RPE–Bruch's membrane flat mounts from 25 eyes, we analyzed 0.4-µm z-stack epifluorescence images of RPE stained with phalloidin for actin cytoskeleton. Using a custom ImageJ plugin, we classified cells selected in a systematic unbiased fashion in six phenotypes representing increasing degrees of pathology. For each cell, area, AF intensity, and number of Voronoi neighbors were compared with phenotype 1 (uniform AF, polygonal morphology) via generalized estimating equations. We also analyzed each cell's neighborhood.

Results. In 29,323 cells, compared with phenotype 1, all other phenotypes, in order of increasing pathology, had significantly larger area, reduced AF, and more variable number of neighbors. Neighborhood area and AF showed similar, but subtler, trends. Cells with highly autofluorescent granule aggregates are no more autofluorescent than others and are in fact lower overall in AF. Pre-aggregates were found in phenotype 1. Phenotype 2, which exhibited degranulation despite normal cytoskeleton, was the most numerous nonhealthy phenotype (16.23%).

Conclusions. Despite aggregation of granules that created hyperAF aggregates within cells, overall AF on a per cell basis decreased with increasing severity of dysmorphia (abnormal shape). Data motivate further development of subcellular resolution in clinical fundus AF imaging and inform an ongoing reexamination of the role of lipofuscin in AMD.

Keywords: retinal pigment epithelium, age-related macular degeneration, autofluorescence, lipofuscin, cytoskeleton, morphometry, Voronoi statistics

Age-related macular degeneration (AMD), the main cause of central vision loss among older adults in industrialized countries, is not treatable for most patients who have it. Metabolic status of the retinal pigment epithelium (RPE), key cells in AMD progression, is visible clinically through fundus autofluorescence (FAF) imaging for retinal disease diagnosis and management.[1] Advanced FAF technologies now include quantitative FAF,[2] fluorescence lifetime,[3] widefield,[4] and adaptive optics–assisted FAF.[5] FAF interpretation is facilitated if comprehensively contextualized by optical coherence tomography (OCT),[6] which discloses subcellular detail of not only RPE but also the tissue layers internal and external to RPE that impact the autofluorescence (AF) signal available for detection.

The strongest FAF signal on excitation with 440 to 510 nm wavelength light comes from RPE lipofuscin (L), with a small (10%) component of melanolipofuscin (ML).[7–10] L are autofluorescent, long-lasting inclusion bodies of lysosomal origin that are characteristically detectable in human RPE at birth and accumulating throughout adulthood. ML contain melanin surrounded by lipofuscin fluorophores.[7,11] The main fluorophores responsible for FAF imaging are visual cycle byproducts of the bisretinoid family that originate in photoreceptor outer segments and enter RPE via daily phagocytosis.[7,12] N-retinylidene-N-retinylethanolamine (AE2) is one prominently investigated molecule[13] recently shown to be abundant in peripheral retina[14–19]; bisretinoid discovery and characterization are ongoing.[20]

FAF is a projection image in which signal strength is impacted by factors at subcellular and cellular levels (Fig. 1), as can be deduced from cross-sectional electron microscopy[7,21,22] and high-resolution light-microscopic histology[23–27] of human RPE. Fluorophores in normal adult human RPE in L/ML granules (Fig. 1A)[7,28] are screened from incoming light by melanosomes (Ms), located in the apical cell body and microvilli. HyperFAF (increased signal at the detector) can be caused by a high concentration of L/ML granules (Fig. 1B), a fluorophore mix or intracellular environment that move spectra into detection range (Fig. 1C), positioning of M posteriorly to reduce screening (Fig. 1D), and increased path length of exciting light

Copyright 2019 The Authors

This work is licensed under a Creative Commons Attribution-NonCommercial-NoDerivatives 4.0 International License.

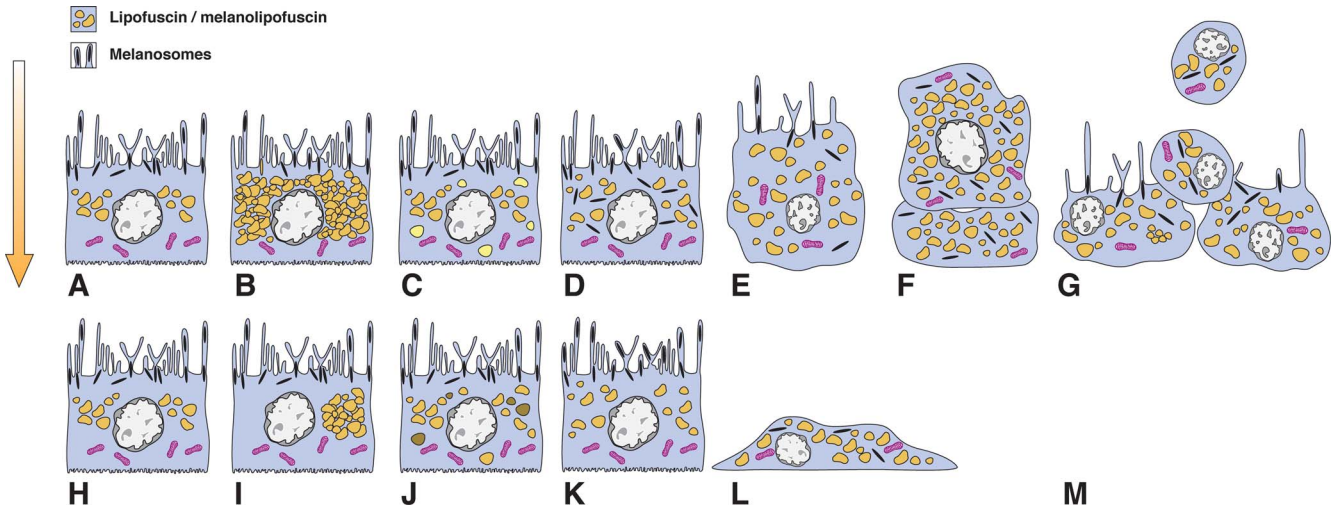

Figure 1. Cellular and subcellular factors influencing autofluorescence signal strength of human RPE**.** Light enters from above (*arrow*) to excite fluorophores within cells. Emissions exit above to be detected by a device (e.g., fundus camera or scanning laser ophthalmoscope). Factors causing hyperautofluorescence (greater signal strength) are shown in (**A**–**G**) and hypoautofluorescence (lesser signal strength) in (**H**–**M**). The combined L/ML population is shown. (**A**) Normal cell contains multiple fluorophores in L/ML, screened anteriorly by M in apical processes and apical cell body (**B**) Higher concentration of L/ML granules. (**C**) Altered mix of emitted spectra, either due to a different fluorophore mix or changes in the fluorophore environment (e.g., altered lysosomal pH) that move more spectra into device detection. (**D**) Basolateral positioning of M to reduce screening (as in aging).[22] (**E**) Taller individual cells (e.g., due to rounding)[23,29] that increase the path length of exciting light through fluorophores. (**F**) Stacking of cells lengthens the light path through fluorophores.[23,29] (**G**) Anterior migration of cells lengthens the light path through fluorophores.[23,25,29] (**H**) Normal cell. (**I**) Redistribution of L/ML leaving cytosol devoid of granules, due to degranulation (empty cytoplasm on the left) or aggregation (clustered organelles on the right).[25,26] (**J**) Altered mix of emitted spectra, either due to different fluorophores or changes in the fluorophore environment that move spectra out of device detection range. (**K**) Apical positioning of M to increase screening (as under the fovea).[94] (**L**) Flattened RPE, shortening the light path through fluorophores.[23] (**M**) Absent RPE.

through cells that are taller individually or vertically superimposed due to stacking or anterior migration (Fig. 1E–G, respectively). Conversely, hypoFAF (reduced signal) can be caused by redistribution or loss of L/ML (Fig. 1I), a different fluorophore mix, or change in environment that moves spectra out of detection range (Fig. 1J), positioning of M to increase anterior screening (Fig. 1K), flat cells with short path length for light (Fig. 1L), and absent RPE (Fig. 1M). Physical and chemical factors not shown in Figure 1 include spectral characteristics and excitation efficiency of biologic fluorophore(s) and efficiency of the detector for specific wavelengths. Tissue-level factors not shown in Figure 1, to be explored in separate reports, include retinal topography[8,10] and screening by overlying features.

Histology relevant to FAF imaging in human eyes with AMD[10,25,29,30] suggest several RPE fates en route to atrophy. Cells can lose L/ML individually by degranulation and or in groups by aggregation followed by basolateral shedding of granule aggregates, phenomena seen to date only in AMD tissues and not in healthy aging.[10] Another is anterior migration, in which nucleated and fully pigmented cells round up, slough off the RPE layer, and migrate into the retina, especially around the border of geographic atrophy.[31–34] The latter represent stages of hyperpigmentation (color fundus photography)[35] and hyperreflective foci (OCT),[36] major intraocular risk factors for AMD progression. A third potential pathway is vitelliform lesions, that is, subretinal hyperreflective and hyperFAF material[37] that may represent extruded RPE organelles and outer segment debris.[26,38] In early AMD, clinical quantitative AF imaging (i.e., with an internal reference standard) shows overall reduced signal.[39,40] These data thus suggest that L/ML loss in the RPE layer rather than gain is associated with AMD, contrary to long-standing expectations.[41]

In this survey of flat-mounted human donor eyes with AMD, we describe and quantify distinct phenotypes of RPE cell morphology and histologic AF. We take a cellular demographics approach that borrows concepts from population-based epidemiology (i.e., treating the RPE layer as a population with more normal cells than abnormal cells), all viewed at one time point. We used systematic sampling to increase the probability of detecting early stages and to reduce bias in estimating phenotype frequency. Our analysis approach assumes that AMD progresses along defined pathways that can be informed by the proportion of cells at any one stage. Our model of AMD progression based in histopathology, clinical imaging, and cell biology[42–47] is that RPE dysfunction begins locally over sub-RPE pathology and expands outward. Our goals were to identify plausible precursors to degranulation and aggregation, and provide histologic guidance for metrics of FAF imaging beyond signal intensity.

Methods

Compliance

The institutional review board at the University of Alabama at Birmingham approved this study. All procedures adhered to the tenets of the Declaration of Helsinki.

Overview

This study analyzed epi-fluorescence images of RPE flat mounts that were captured in a systematically unbiased fashion for our published survey of RPE cytoskeleton and histologic AF in 25 AMD eyes[25] (see Supplementary Material for methodologic details). For this quantitative study of the same AMD eyes, each individual RPE cell was represented as a Voronoi region[48,49] after assignment of cell centers (see Supplementary Material). Total AF intensity in projection images of z-stacks, the number of neighbors, and cell area were automatically quantified by custom software.[10] To these quantitative data we added semiquantitative

Table 1. Morphology and AF Pattern Phenotype Criteria

Phenotype Classification	Criteria/Rules
Morphology	
Ungradable	Cell border is undetectable or cut off by image edge.
Polygonal	Cell borders have vertices and mostly straight edges; many cells have brush-like apical surface (Fig. 3A).
Round	Circular or oval cells with no vertices.
Mixed	At least one vertex and at least one edge that is rounded rather than straight, including cells that appear "bloated".
Misshapen	Cell is definitely present and not cut off by image edge, but the shape is indeterminate (blurred/faint cytoskeleton staining, partial discontinuity of cytoskeleton, actin "junk") or does not fit into other morphology categories.
Concave	At least one edge with a significant concavity.
AF pattern	
Ungradable	Ungradable morphology making AF pattern determination within cell borders impossible, or AF return was so blurry pattern could not be discerned.
Unremarkable	Roughly even and uniform AF granules throughout the area of the cell, except when blocked by nucleus.[93]
Degranulating	Areas of no AF return not due to nucleus.
Aggregating	Delimited, roughly spherical, area of dense AF granule packing; often, but not always, more intense AF return than rest of cell.
Aggregating and degranulating	At least one aggregate and one area of degranulation present.
Empty	Completely devoid of AF granules.

judgments of a trained observer about AF patterns and cellular morphology, within the same Voronoi regions.

Although it is possible that removing the retina from RPE–Bruch's membrane flat mounts also removed apical portions of RPE, thus impeding accurate assessment of cellular AF, our experience with histology of postmortem eyes suggests this possibility is unlikely. The most common artifacts are detachment of outer segments from RPE that may or may not take RPE apical processes with them (e.g., figure 5 of Ref. 32), detachment of inner segments at the myoids (bacillary layer detachment),[50] and detachment of RPE from Bruch's membrane at sites of basal linear deposit and soft drusen.[51,52] We do not see in histology splits through the middle of RPE suggesting that only the basolateral half of cells are present in flat mounts. We assume that these artifacts are stochastic and that their impact on our results is minimized by choosing images in the way we did. We did see in flat mounts many cells with melanosomes, or a brush-like appearance of the phalloidin signal, consistent with intact cell bodies and apical processes (see Results). Finally, cells were imaged in apical-to-basal z-stacks of a constant number at each specific location.

Imaging Data Analysis

From the original image dataset of 1585 images, a set of 400 total images (17 from each eye or until usable images from an eye were depleted) was chosen with a random number generator. We pooled images across three regions (fovea, perifovea, and near periphery), despite regional differences in cell area,[10] because the RPE layer was absent in many areas in central macula of AMD eyes, and our categorical analysis of phenotypes did not depend on cell size. The center of each RPE cell was defined manually in images of phalloidin-labeled RPE by trained observers (AVZ, TA, JM) using a custom FIJI plugin (Find_Centers)[53] and a digitizing tablet (Intuos; Wacom, Saitama Japan). The resulting Voronoi diagrams qualitatively agreed with actual RPE cell geometry by visual inspection. This procedure contrasts with that used in our previous study of normal eyes,[10] in which consistent RPE morphology allowed semiautomated assignment of cell centers by the same plugin. To ensure the validity of Voronoi analyses, we defined in each image a central area that had at least one row of cells between it and the image edge (details in supplementary figure 3 of Ref. 10). A custom FIJI plugin ("AF Phenotypes," Fig. 2, available on request) generated a scrollable z-stack of successive images. A single trained observer (JAG) assigned morphology and AF distribution pattern phenotypes (Table 1, Fig. 3). Classifications were repeated at one location from each eye to determine intraobserver repeatability (morphology weighted kappa = 0.9708; AF Pattern weighted kappa = 0.9770). Area, AF intensity,[10] and number of neighbors (NN) was automatically measured via custom FIJI software (KRS) for each Voronoi region. AF intensity was quantified in arbitrary units and normalized to the mean value of phenotype 1 cells in the same eye, which were considered healthy (see below), to control for differing background AF between imaging sessions unrelated to inherent RPE AF.

Generalized estimating equations were used to compare variables by cellular phenotypes while accounting for repeated measures, the Poisson distribution was used for count data, and the normal distribution was used for continuous data. We did not stratify data by age, severity of AMD, or retinal location because of the relatively few occurrences of diseased phenotypes. Concave cells (defined below) were excluded from all analyses except frequency, because concavity violates assumptions of Voronoi analysis. Cells considered ungradable for either morphology or AF distribution were excluded from all analyses. Phenotype categories were pooled for statistical tractability (Table 2). With these methods, it can be assumed that the most frequently found category is "normal" (i.e., healthy), and categories increase in abnormality (i.e., disease) as frequency decreases. Accordingly, we numbered phenotypes (Ph) 1 to 6 in order of decreasing abundance and increasing pathology.

Our model of locally driven AMD progression suggests that neighbors will be similar to each other, at least at the extremes of all normal and all degenerating. For intermediate phenotypes, neighbors may exhibit high variance. Thus, we also analyzed for each cell its "neighborhood" of Voronoi neighbors. We defined a neighborhood as the cells immediately adjacent to a central reference cell. To eliminate incomplete neighborhoods from analysis, cells without at least one cell center between it and the image edge were not used as a reference. For each phenotype, mean neighborhood area and AF intensity were measured, as well as the average frequency distribution of neighbor phenotypes.

Results

A total of 400 images in 25 eyes (questionable/early AMD: 18; late nonexudative AMD: 2; late exudative AMD: 5) were surveyed (23 eyes, $n = 17$ images; 1 eye, $n = 5$ images; 1 eye, $n = 4$ images). After excluding concave or cells considered ungradable for either morphology or AF, a total of 29,323 cells were analyzed for frequency, area, AF intensity, NN, and neighborhood characteristics (Figs. 4–6). Cell phenotype frequencies are shown in Figure 4A. The healthy Ph 1 was

Investigative Ophthalmology & Visual Science

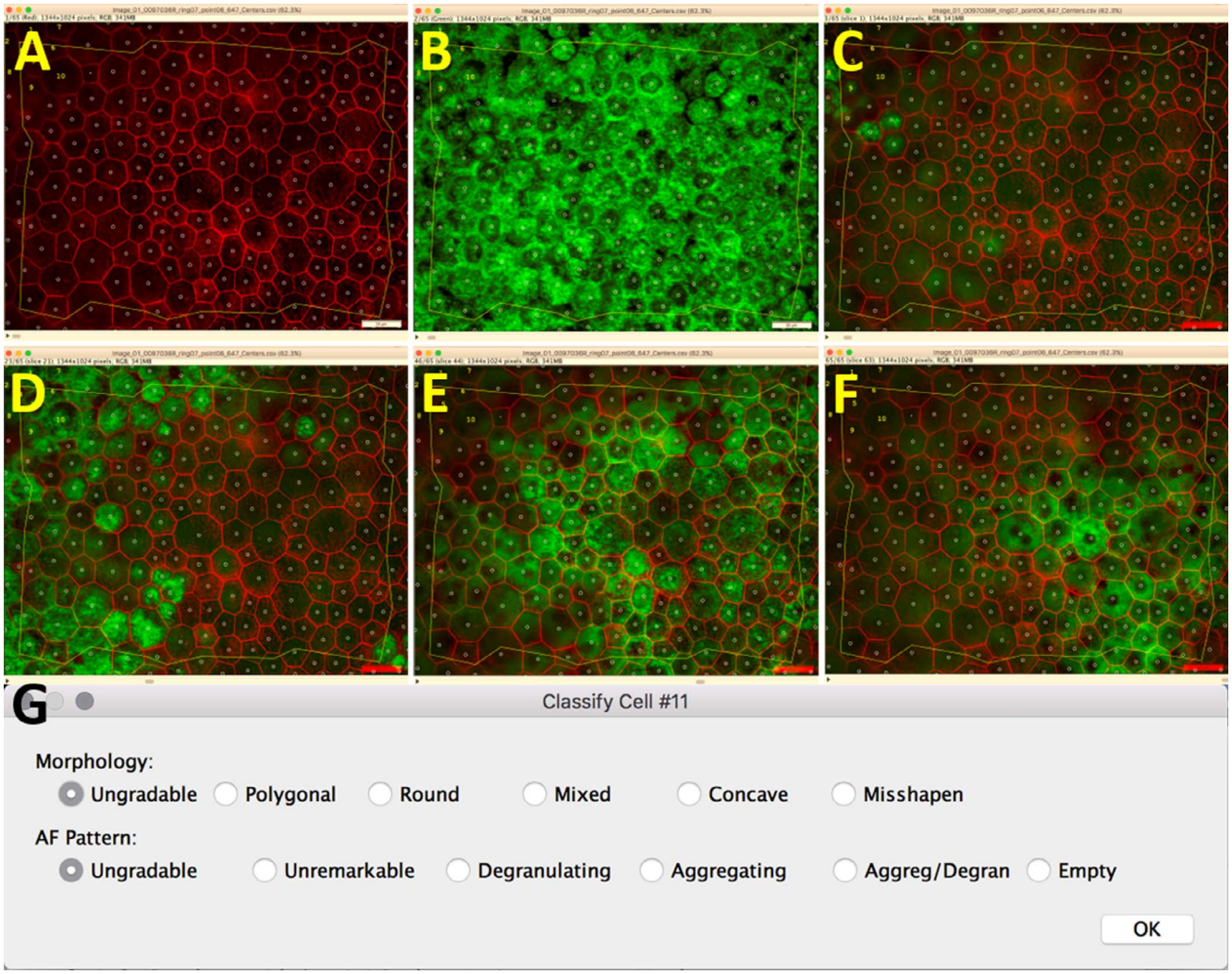

Figure 2. Demonstration of the custom FIJI plugin "AF Phenotypes." Input to the plugin was an image stack. Image 1 (**A**) of the stack was cytoskeleton labeled with 647 Alexa-conjugated phalloidin. Image 2 (**B**) was a projection all-in-focus image of confocal autofluorescence, at excitation wavelength of 488 nm. Images 3-n (**C–F**) were the 0.4-µm apical-to-basal planes of the z-stack, overlaid by the cytoskeleton image. A single trained observer (JAG) assigned morphology and AF distribution pattern phenotypes (Table 1, Fig. 3). Phenotypes were assigned by selecting a single radio button from a menu (magnified in **G**) for both parameters of the "current cell," denoted by a *yellow dot* at the cell center. All cells yet to be classified were denoted by a *small white circle* in the cell center. Cells that were already classified were denoted by a sequence number placed at the cell center. The plugin also featured a zoom-in/out feature and a 20-µm scale bar in the lower right-hand corner. On completion of each image for a given location, the plugin generated a .csv file containing cell numbers with assigned phenotypes and a .tif file of the z-stack for reference.

much more abundant (80.74%) than the less healthy Phs 2 to 6. Although far less abundant than Ph 1, Ph 2 was also notably more abundant than Phs 3 to 6, each constituting a minor portion of RPE cells in AMD eyes (<2% each, <5% total).

Of other cell characteristics, most common were clumped AF granules that could be considered pre-aggregates (Fig. 7). Although not as compact, spherical, or sharply bordered as aggregates (Fig. 7A), pre-aggregates appeared separate from the surrounding uniform distribution. Without areas of degranulation or obvious aggregates, the AF pattern of cells with pre-aggregates was considered unremarkable. As described,[25] other common occurrences included cytoskeletal stress (e.g.,

Table 2. Pooled Phenotypes for Statistical Analysis

Category	Morphology	AF Pattern
Ph 1 (healthy)	Polygonal	Unremarkable
Ph 2	Polygonal	Degranulating/Empty
Ph 3	Round/Mixed/Misshapen	Unremarkable
Ph 4	Polygonal	Aggregating and Aggregating/Degranulating
Ph 5	Round/Mixed/Misshapen	Degranulating/Empty
Ph 6	Round/Mixed/Misshapen	Aggregating and Aggregating/Degranulating
Ph 7	Concave	All

Investigative Ophthalmology & Visual Science

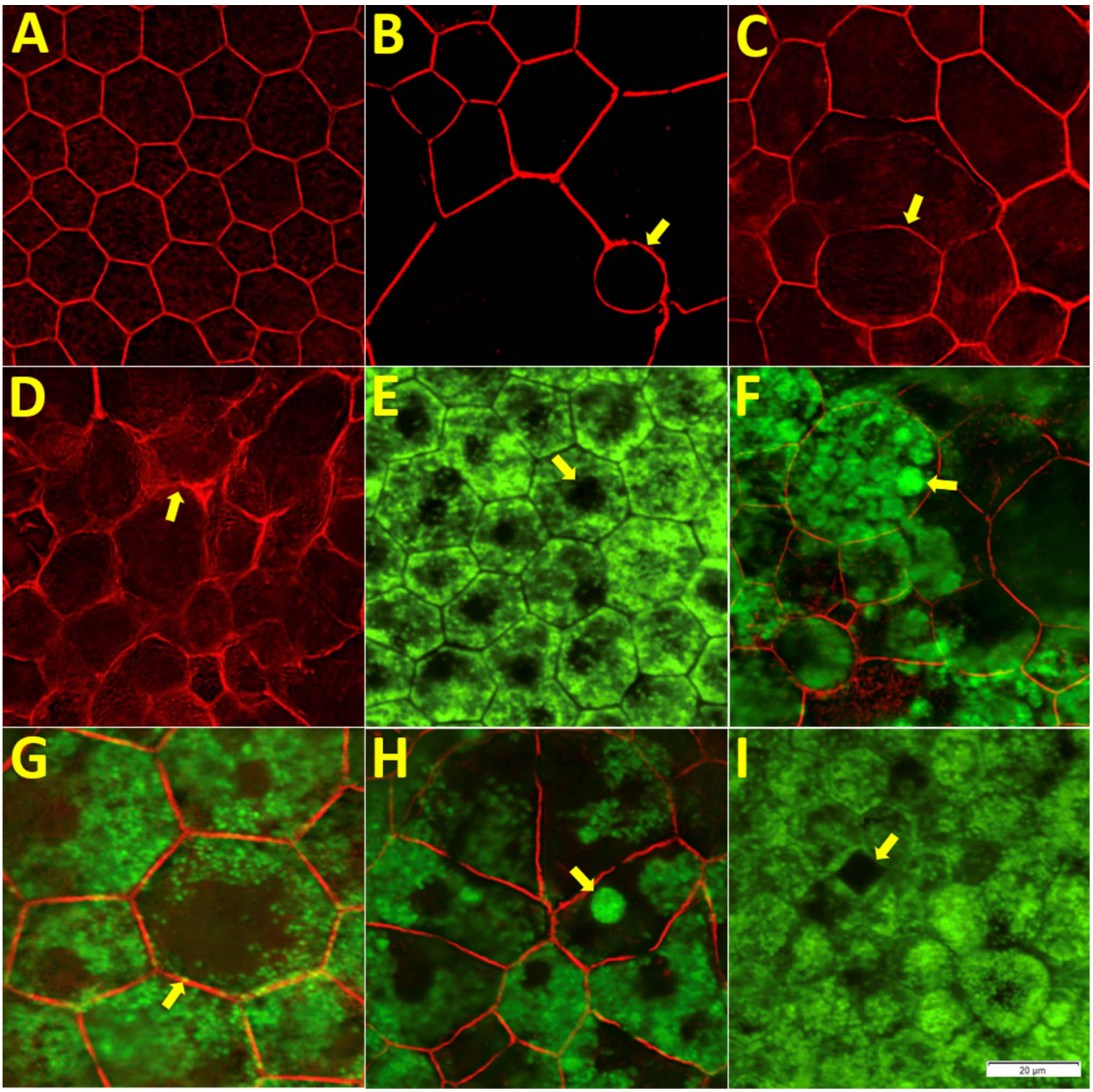

FIGURE 3. Morphology and AF phenotypes: (**A**) Polygonal, (**B**) Round, (**C**) Mixed, (**D**) Misshapen, (**E**) Unremarkable AF (*white arrow* shows hypofluorescent area of a nucleus), (**F**) Mixed, Aggregating AF, (**G**) Polygonal, Degranulating AF (**H**), Mixed, Aggregating-Degranulating AF, (**I**) Polygonal, Empty AF. *Scale Bar*: 20 µm.

splits and interruptions), barrel-shaped cells, sub-RPE deposits, bi/multinucleation, and atrophy. Bi-laminar RPE, mushroom cells, and concave cells were repeatable[25] but infrequent. Bi-laminar RPE, in which one layer of actin cytoskeleton could be seen overlying another, was seen in 3 of 400 images (<1% of gradable cells).[23] Mushroom cells that extrude a portion of granule-filled cytoplasm into the outer segment layer while remaining rooted in the continuous RPE layer are seen in 27 of 400 images (<1% of gradable cells) and were scored according to their bases in the layer of RPE cell bodies.

Mean cell area stratified by phenotype is shown in Figure 4B. Ph 1 (healthy) was significantly smaller ($P = 0.0416$) than Phs 2 to 6 (less healthy). There was a trend of increasing cell area with increasing pathology. Despite this trend, Ph 1, which has the smallest mean area and spacing, also has the largest maximum area by almost 1000 µm^2 and largest maximum spacing by almost 10 µm (Table 3). We attribute this to the much larger sample size of Ph 1 cells, and, thus, more outliers outside 2 SDs of a normal distribution.

Mean normalized AF intensity stratified by phenotype is shown in Figure 4C. Ph 1 had a significantly higher ($P = 0.0008$) AF intensity than Phs 2 to 6. This appears to be an effect of Phs 2 and 5, in which areas of degranulation caused notably lower AF intensity. Aggregates do not increase AF intensity of individual cells, despite appearing brighter, either because aggregates are too small, they are associated with degranulation that cancels out any focal increase of AF, or both.

Investigative Ophthalmology & Visual Science

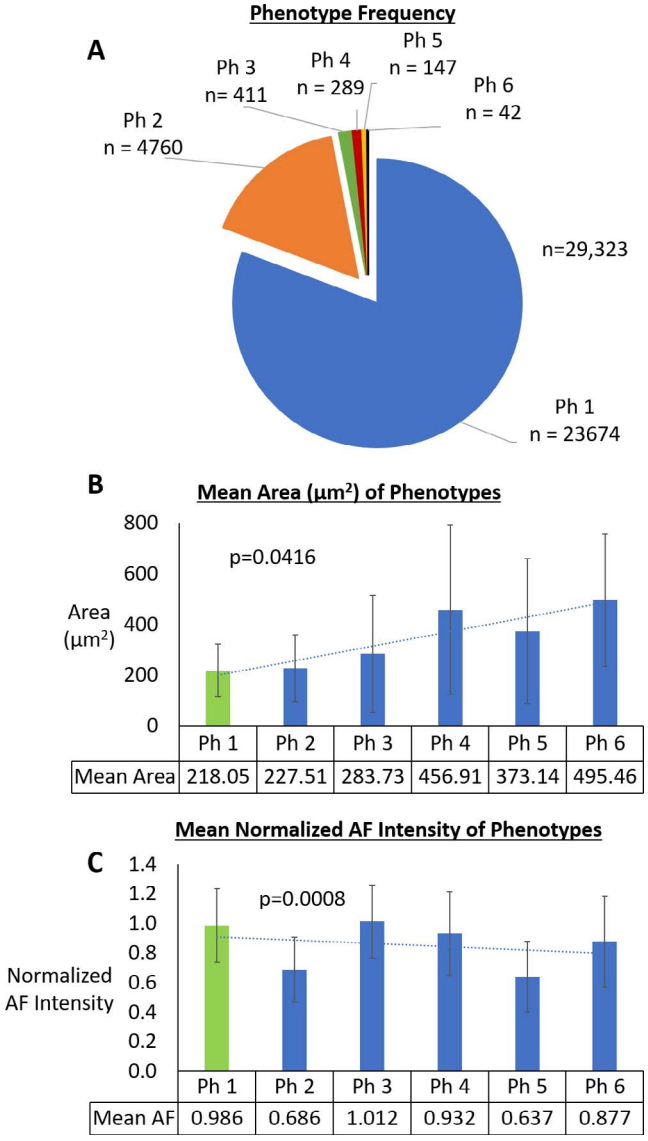

Figure 4. Frequency, area, and AF intensity of RPE phenotypes. (**A**) Ph 1 (healthy) was by far the most abundant. Ph 2, although far less frequent than Ph 1, was notably more abundant than the rest of the diseased phenotypes. Phs 3 to 6 each constituted a minor portion (<2% each, <5% total) of RPE cells in AMD eyes. (**B**) Ph 1 had the smallest mean area and was significantly smaller ($P = 0.0416$) and packed tighter than Phs 2 to 6 (unhealthy). (**C**) Phs 1 and 3 (healthy, unremarkable AF) were the most intensely autofluorescent. Phs 2 and 5 (degranulating/empty AF) had notably decreased AF intensity. Ph 1 mean AF intensity was significantly different ($P = 0.0008$) from phenotypes 2 to 6 due to the large number of Ph 1.

NN distribution of each phenotype is shown in Figure 5. All phenotypes most often contacted six neighbors (i.e., 34%–45% per phenotype), somewhat lower than the distributions we previously observed in young and aged normal eyes (mean six neighbors for fovea/perifovea/periphery 59%/50%/45% and 53%/47%/47% for ≤51 and >80 years, respectively).[10] Phs 1 to 5, especially 1 and 2, most often contacted five to seven neighbors. Ph 6 most often contacted six to eight neighbors. NN was more variable with increasing pathology. Poisson distribution regression analysis of NN showed that Phs 2 to 6 contacted significantly more neighbors ($P = 0.0056$) than Ph 1. These findings are consistent with more variable geometric packing of cells in diseased RPE.

Table 3. Cell Areas and Spacing

	Ph 1	Ph 2	Ph 3	Ph 4	Ph 5	Ph 6
Mean area, µm²	218.1	227.5	283.7	456.9	373.1	495.5
SD area, µm²	103.6	131.1	230.7	332.7	284.9	261.5
Mean spacing, µm	15.7	16.0	17.5	22.3	19.9	23.7
SD spacing, µm	3.1	3.6	5.5	7.2	6.9	6.2
Minimum area, µm²	31.5	63.2	69.7	115.3	62.3	164.4
Minimum spacing, µm	6.1	8.1	8.5	11.4	8.4	13.6
Maximum area, µm²	4616.4	3743.2	3180.5	2439.9	1592.8	1404.6
Maximum spacing, µm	75.4	66.2	63.2	57.3	43.6	42.4

Results of neighborhood analysis are shown in Figure 6. Paralleling the overall frequency of phenotypes, Ph 1 was the most frequent neighbor for all phenotypes. However, Ph 1 dominated less of the neighborhood as the status of the reference cell worsened (Fig. 6A). This suggests unhealthy phenotypes are more likely to be surrounded by other unhealthy cells. Furthermore, each phenotype was more frequent in its own neighborhood than in neighborhoods of other reference cell phenotypes. Figures 6B and 6C show the mean area and AF of each phenotype's neighborhood, respectively. Cell areas in a neighborhood expanded with worsening pathology, but in a subtler manner than shown by single-cell analysis. Cell area in a neighborhood anchored by Ph 1 was significantly smaller ($P = 0.0287$) than neighborhoods anchored by Phs 2 to 6. Mean neighborhood AF was significantly higher ($P = 0.0089$) for Ph 1 than for Phs 2 to 6, likely due to the decreased AF surrounding Phs 2 and 5. As with area, the effect was more subtle than single-cell analysis, likely due to the numerous Ph 1 in all neighborhoods skewing means toward healthy values.

Figure 8 shows a commonly observed neighborhood "flower" pattern, in which a central cell enlarged and/or changed shape, with pathology decreasing across successive tiers (typically 1–2) of neighbors. This pattern, along with the frequency of Ph 1 as a neighbor, and subtler changes at the neighborhood level, demonstrate how focal areas of disease are often surrounded by many healthy cells.

Discussion

Identifying the frequency of cells with specific characteristics is an important step in understanding the significance of RPE changes in AMD.[54] Subcellular AF changes in AMD eyes first described by our group[25] were herein extended, providing a firm morphologic basis for future studies designed for molecular discovery. In this study, a trained observer characterized 29,323 RPE cells surveyed in an unbiased manner in flat-mounted tissues, to capture early signs of pathology. Based on a model of factors influencing AF (Fig. 1), our methods were designed to assess intracellular packing of AF organelles within cells of varying shapes (Figs. 1B, 1I). Different morphologies imply different molecular mechanisms of cellular demise and potentially different strategies for cytoprotection and fundus AF readouts for clinical trials.[6] We tested two such phenomena potentially visible in fundus AF (degranulation and L/ML aggregation, Fig. 1I). Other pathways (anterior migration, Fig. 1G; vitelliform, not shown) are both best appreciated in cross-sections of RPE with retina attached rather than in whole mounts of just the RPE–Bruch's membrane complex used herein. Our main findings are a reduction of total cellular AF in cells that contain highly AF aggregates, identification of pre-aggregates as precursors, numerous degranulating cells, and transitional morphologies from a flower pattern seen in aging to frank degeneration.

Investigative Ophthalmology & Visual Science

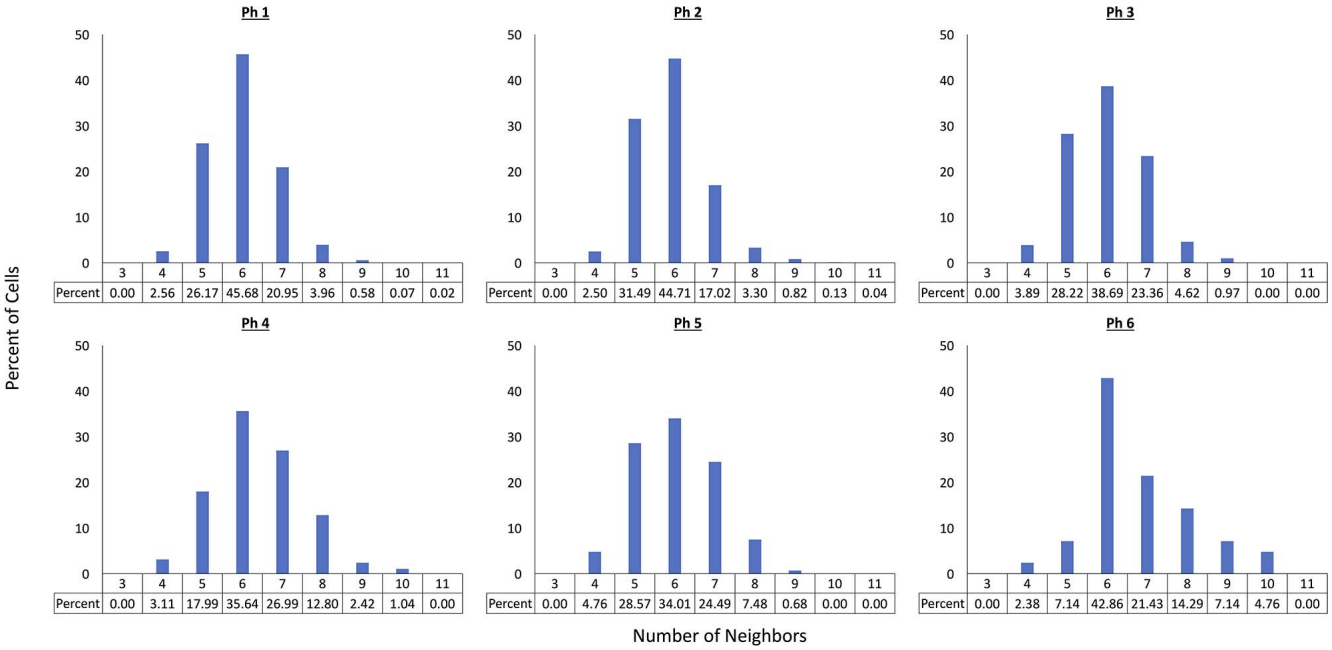

Figure 5. NNs of RPE phenotypes. All phenotypes most often contact six neighbors (34%–45% per phenotype). Phs 1 to 5 most often contact five to seven neighbors. Ph 6 most often contacts six to eight neighbors. There is more variation in NN with increasing pathology. Poisson distribution regression analysis of NN showed Phs 2 to 6 contact significantly more neighbors ($P = 0.0056$) than Ph 1.

Importantly, the earliest RPE changes in AMD eyes include loss rather than gain of AF signal, even before cytoskeletal derangement, consistent with our results in normal aged eyes.[10]

Aggregates are the most hyperAF single features in the RPE layer, due to highly concentrated fluorophore-containing organelles (Fig. 1I) compared with the nearly uniform distribution in healthy cells.[28] Aggregates are strikingly characteristic of Phs 4 and 6 (1.1% of cells combined); yet a key observation of our study was that cells containing aggregates and their neighborhoods were overall less AF than the healthy Ph 1 cells. We attribute this effect to a combination of small aggregate size and the frequent coexistence of degranulation in the same cells. Granule aggregates were first illustrated by the Sarks et al.[31] in electron microscopy and subsequently seen in confocal microscopy ("condensations")[55] and high-resolution bright-field histology.[23] In cross-sectional histology, aggregates are observed not only within cells but also in the extracellular compartment at the basolateral surface of RPE cells, where they are embedded in thick basal laminar deposit close to Bruch's membrane. Such aggregates can be seen by clinical OCT imaging, if large enough and the deposit is thick.[23,56] Thus, we suggested that aggregates within the cell, as seen in this study, are thus fated for basolateral exocytosis in the "shedding" phenotype.[23,25]

Another key finding was the common occurrence of pre-aggregates, defined as organelles more tightly associated than those in the rest of the cytoplasm,[28] but with less distinct boundaries than aggregates. Because pre-aggregates are found in Ph 1 cells, often before obvious cytoskeletal stress, we interpret them as early pathological precursors rather than remnants of definitive aggregates. Several possibilities exist for formative mechanisms of aggregates and pre-aggregates. Cytoskeleton is essential for organelle transport,[57–60] and we could evaluate cytoskeletal dysfunction with phalloidin binding. However, cytoskeletal stress was far more frequent than aggregates and pre-aggregates, suggesting that these phenomena are not directly related. In human fibroblasts, cross-linking molecules cause lysosomal aggregates to fuse,[61] similar to a physiologic process in RPE lysosomes,[62] so the presence of cross-linking molecules could play a role. Finally, AMD RPE exhibits increased levels of apoptosis-suggestive TUNEL-positive cells,[63] apoptotic marker Caspase-8, and *Alu* RNA that may have transcriptional or cytotoxic roles.[64,65] Thus, aggregates might be apoptotic bodies.[66] Further investigation is needed to elaborate on these hypotheses.

Ph 2 involves nonvisibility of individual AF granules, and at 16.23% of the total cellular population, is the most abundant of the diseased phenotypes. Although we cannot distinguish with absolute certainty true degranulation from accumulation of non-AF materials without special staining methods,[28] z-stack scrolling during data collection minimized this possibility (Supplementary Fig. S2). The healthy cytoskeleton of Ph 2 supports the idea that aggregate shedding is a negligible factor in their appearance. Further, Phs 2 and 1 (227 μm^2 and 218 μm^2, respectively) have notably smaller areas than the cells with aggregates (Phs 4 and 6, 456 μm^2 and 495 μm^2, respectively). If Ph 2 cells arose from the shedding of aggregates, it is hard to explain this 2-fold difference in size. The most likely explanation for Ph 2 appearance is dispersal of individual granules to the extracellular space, where they may be ingested by neighboring cells. RPE L/ML are found in drusen[67,68] and in the Henle fiber layer (figure 7 of Ref. 33; supplementary figure 3 of Ref. 69) of AMD eyes. Finally, the abundance of Ph 2 cells suggests that they progress more slowly than do other phenotypes. If our logic is correct, then the Ph 2 cells are following a third, distinct RPE death pathway in AMD that was underappreciated in our previous survey of cross-sectional histology.[23]

Systematic unbiased sampling also uncovered a localness of AMD pathology, exemplified by evolution of a flower-like pattern of a central cell ringed by neighbors (Fig. 7). An orderly pattern in normal eyes,[10] this formation appears to progress in AMD eyes to cytoskeletal disintegrity and dysmorphia (abnormal shape). The central cell is often multinucleate, suggestive of fusion, or more likely, failed cytokinesis,[70] perhaps a

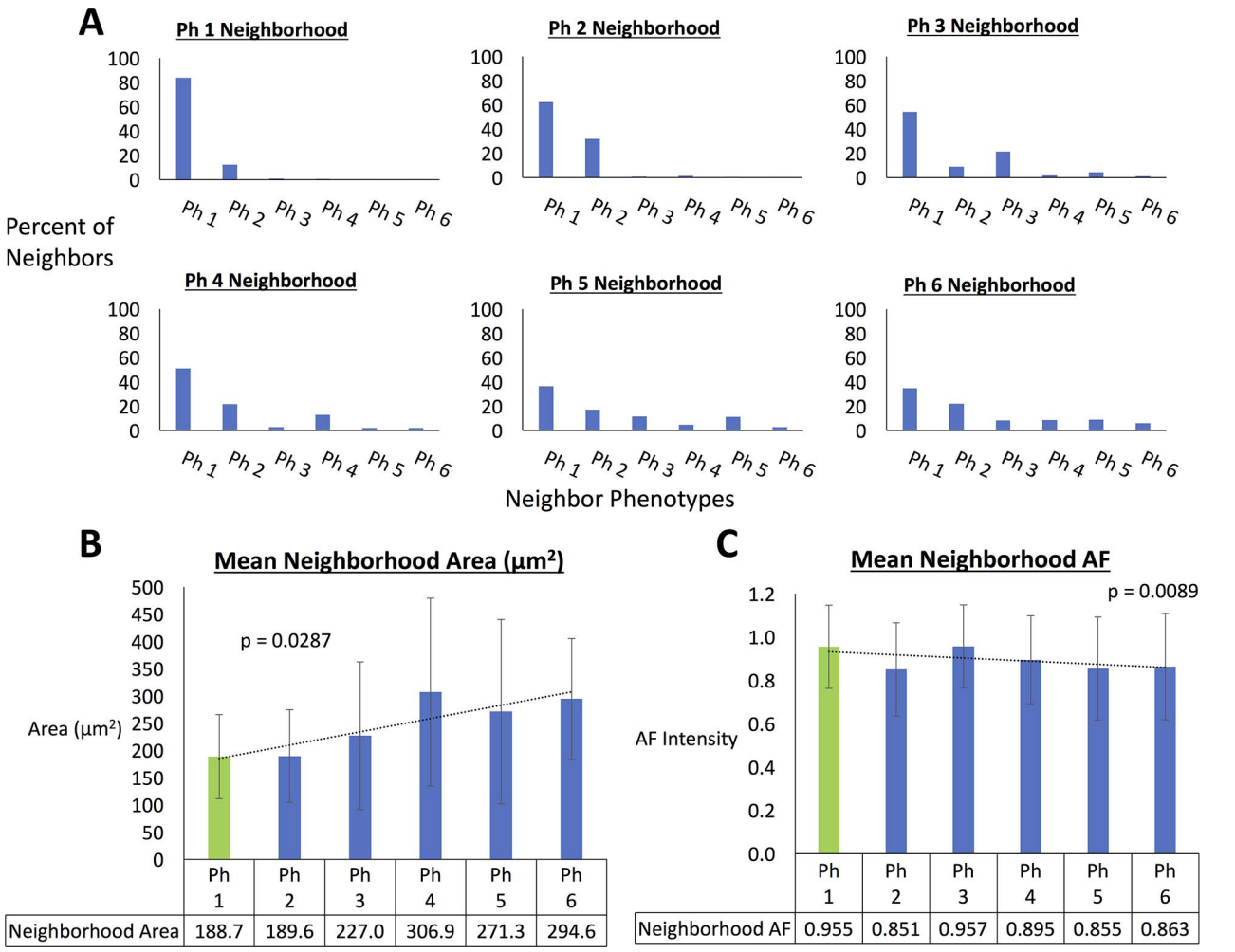

Figure 6. Neighbor frequency distribution becomes more variable as pathology increases, whereas mean neighborhood area and AF show subtler trends than individual phenotype values**.** (**A**) Neighbor phenotype proportions for the average neighborhood of each reference cell phenotype. In conjunction with the overall frequency of phenotypes, Ph 1 was the most frequent neighbor for all phenotypes. Neighbor frequency distribution was more variable as reference cell phenotype increased in pathology, and Ph 1 dominated less of the neighborhood. This suggests unhealthy phenotypes are more likely to be surrounded by other unhealthy cells. (**B**) Mean area of cells in a neighborhood increases with increasing pathology, and Ph 1 neighborhood area is significantly smaller ($P = 0.0287$) than Phs 2 to 6 neighborhoods. The trend is more subtle than single-cell analysis. (**C**) Ph 1 mean neighborhood AF intensity was significantly greater than Phs 2 to 6, due in large part to Phs 2 and 5 (degranulating/empty). The effect was more subtle than single-cell analysis.

proliferative response to local injury. If we had analyzed only areas of obvious abnormality, foci of early change among the mostly healthy cells (Fig. 6) would have been missed. This is important, because quantification of individual cell morphology has promising potential for identification of early pathological change.[71,72] Reasons behind localness were not addressed in this study, but the presence of underlying drusen and basal laminar deposits[30,46,69] that expose RPE to proinflammatory lipid while also increasing diffusion distance from the choriocapillaris is one obvious possibility. Similar cytoskeletal changes also occur in several mechanistically distinct mouse models,[64,65,71,73,74] suggesting a common response to many insults.

Our evidence that the RPE layer becomes less AF in concert with reduced AF organelle content indicates that these cell-autonomous changes are causal, supporting recent clinical quantitative AF imaging studies that found decreased rather than increased FAF intensity with AMD.[39,40] As in our study of aging RPE,[10] we did not find cells with markedly increased AF intensity (Fig. 1B), which was expected if RPE cells engorged with L/ML preceding death, as postulated.[31,75] Focally increased signal in clinical fundus AF is currently best explained by vertically enlarged, stacked, or anterior migrating RPE (Figs. 1E–G) that in a projection image are superimposed on the RPE layer.[29,34] By high-resolution histology and electron microscopy, these ectopic cells are nucleated and fully granulated RPE,[26,38] consistent with in vivo OCT showing hyperreflective foci arising from the RPE layer.[27]

Collectively, our data with others indicate that contrary to widely held theories, L/ML may not be harmful in AMD. One theory suggests that L/ML are phototoxic, yet retinal illuminance is uniform well beyond the 21° diameter macula,[76,77] and epidemiologic data do not support lifetime sunlight exposure as an AMD risk factor.[78,79] This same theory builds on the deleterious effects of treating cultured cells with bisretinoid fluorophore A2E, yet this L/ML component is reliably lower in macula than in peripheral retina,[43–48] a distribution not detectable in early studies analyzing whole eyecups.[80] A report that age-related photoreceptor and RPE loss correlated to histologic AF used spatially imprecise morphometry,[81] whereas by using computer-assisted analysis of retinal flat mounts, we confirmed that AF crests at the

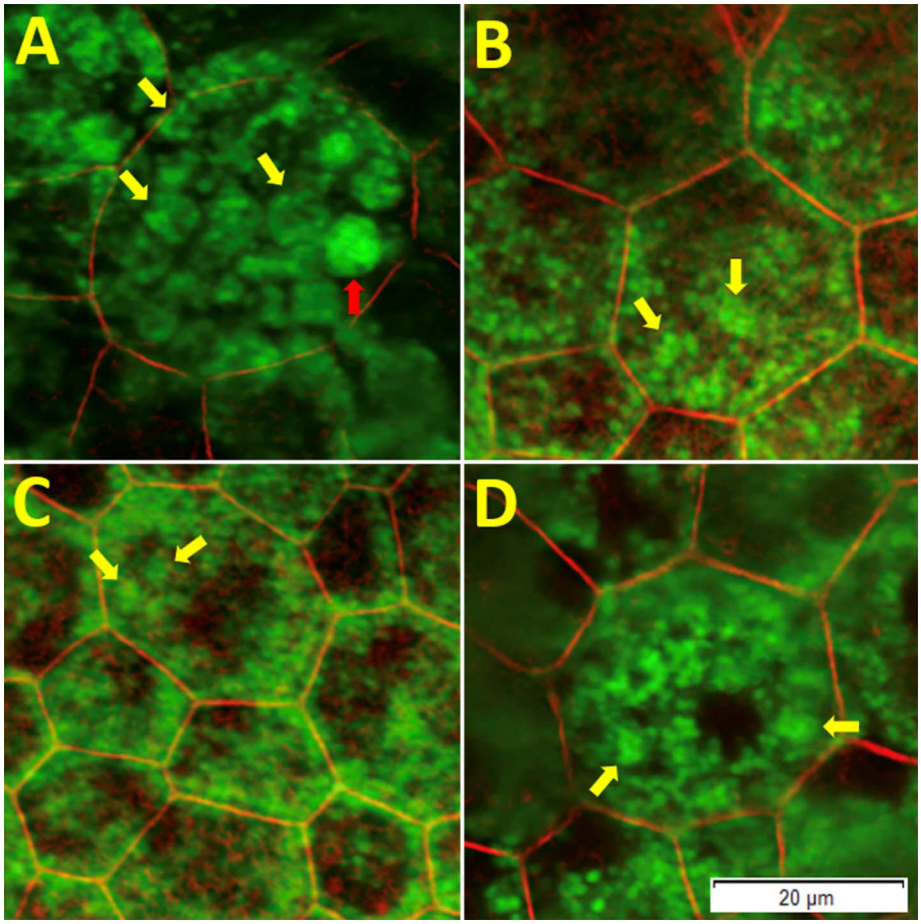

Figure 7. Pre-aggregates of autofluorescent granules in RPE of AMD eyes. (**A**) *Red arrow* shows a definite aggregate. (**A–D**) *Yellow arrows* show proposed pre-aggregates, that is, clumps of AF granules that were not as concentrated or sharply delimited as definite aggregates.

macular edge like rod photoreceptors[8,10] and demonstrated that rods die before cones in central macula,[82] where soft drusen precursors accumulate.[83] Consideration of L/ML toxicity motivated visual cycle modulators as therapeutic agents for AMD, for which clinical trials have not only failed to prevent progression, but also exacerbated visual dysfunction.[84,85] In contrast, night vision is improved by short-term high-dose supplementation with vitamin A.[86,87] From our perspective, more new data to explore the role of L/ML in outer retinal retinoid balance would be most welcome. Humans and nonhuman primates will be especially valuable, because A2E and histologic AF are spatially correlated in mouse RPE[33] (i.e., a notable biologic dissimilarity to human macula).

Beyond quantitative AF, our data are relevant to in vivo fundus AF imaging by current and emerging technologies. Whether single cells or cells with subregions of simultaneous degranulation and aggregation (Fig. 3H) are visible clinically depends on factors that reduce optical sampling relative to pixel sampling. These include lateral point spread function (i.e., 3-dimensional image of a point-like object), which in turn depends on the eye's optical properties (aberrations), pupil size, and diameter of the illuminating beam. In the commercially available Heidelberg Retinal Angiograph and Spectralis, pixel sizes in the eye are 4.8 µm, that is, smaller than individual RPE cells (Table 3). Even if Nyquist sampling is taken into account,[88] within-cell variability as we observed might be visible in vivo, perhaps by adaptive optics–assisted FAF imaging.[5,89,90] This technology uses short (532 nm) and long (796–850 nm) wavelengths to excite presumed bisretinoids and melanin, respectively, and reveals tiled hexagonal elements with RPE-like spacing and spatial density. Open questions are whether emissions at both wavelengths arise from the same subcellular sources (e.g., M/L),[22,28] and what accounts for non-AF cell centers that appear larger than RPE nuclei in histology.[28,91,92] These questions will benefit from our ongoing studies using volume electron microscopy of human RPE[28] to account for all organelles of imaging significance. Nevertheless, our model (Fig. 1) and illustrations (Figs. 3, 7, 8) represent potential visualization targets for these advanced imaging techniques.

Strengths of this study include the robust sample of 29,323 human RPE cells in 25 AMD eyes preserved $\leq$4.2 hours after death, unbiased sampling for improved RPE demographic description, virtual 0.4-µm-step z-stack scrolling to visualize L/ML within individual cells, discrete phenotype categories, and good intraobserver repeatability. Limitations include lack of clinical information for eye donors, loss of some RPE apical processes and subretinal drusenoid deposits[93] during tissue preparation, lack of cell height data, inability to account for out-of-layer factors and other in vivo AF-influencers, not separately analyzing macular subregions, lack of molecular identification techniques, and lack of specific visualizations for non-AF nuclei and melanosomes. Nevertheless, this is the first quantitative study of RPE morphology and subcellular AF patterns in donor eyes with AMD. These phenotypes can be used to identify areas of potential disease progression in eyes that appear healthy at the fundus level. These data improve the subcellular basis of clinical AF, support a reexamination of the

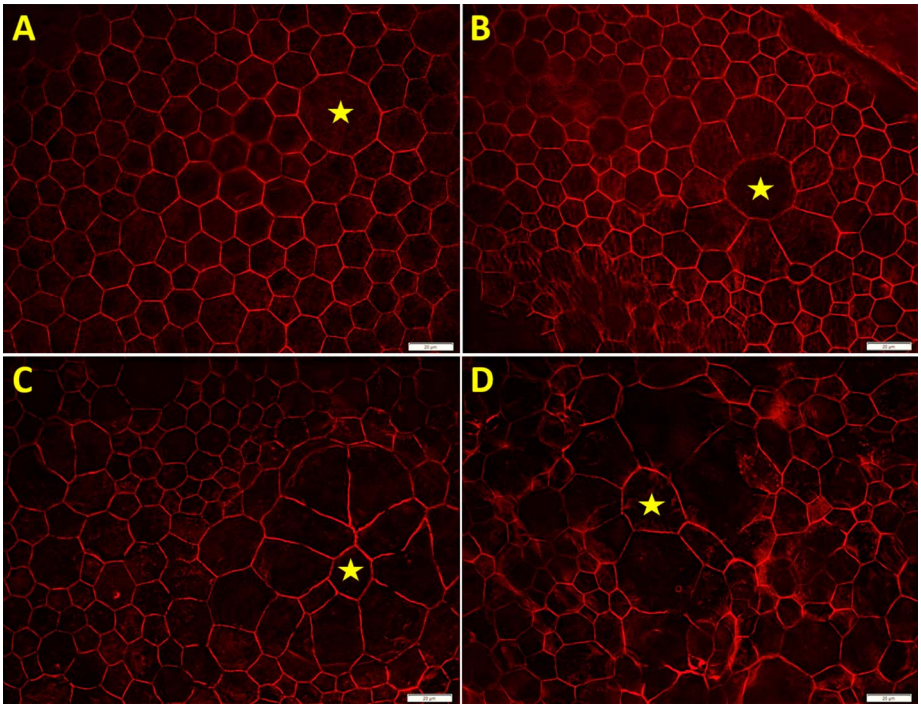

Figure 8. Focality of change in RPE morphology**.** At lower magnifications than those used in Figure 2, areas of largely healthy RPE are seen to include areas of notable change as small as a few cells. Many images contained both healthy RPE and diseased cells. Sampling only areas of disease obvious at a lower magnification can miss focal changes suggestive of early disease. (**A**) A regular, healthy appearing RPE layer with numerous polygonal cells. A distinct reference cell (*star*) is significantly larger than the others, yet it maintains a polygonal shape. (**B**) A mostly healthy appearing RPE layer; however, a reference cell and its neighbors are all appreciably larger than the others while still polygonal. (**C**) A reference cell (*star*) with neighbors that are enlarged polygons and mixed. Some second-tier neighbors also depart from polygonal. (**D**) A large reference cell (*star*) with large neighbors. The entire field of view contains irregularly sized and shaped cells, most of which exhibit stress fibers, actin fraying, or mushrooming.[25] *Scale Bars*: 20 μm.

role of lipofuscin in AMD, further motivate the development of cellular resolution imaging, and suggest variability in internal structure, size, and NN as metrics for clinical and preclinical AF studies.

Acknowledgments

Presented at the annual meeting of Association for Research in Vision and Ophthalmology, Honolulu, Hawaii, United States, April 2018.

The authors thank David Fisher for graphic design of Figure 1.

Supported by National Institutes of Health (Bethesda, MD, USA) Grants T35HL007473 (JAG), R01EY027948 (TA, CAC), and R01EY015520 (CAC); Research to Prevent Blindness (New York, NY, USA) (CAC); EyeSight Foundation of Alabama (Birmingham, AL, USA) (CAC); International Retinal Research Foundation (Birmingham, AL, USA) (CAC); German Research Foundation (Bonn, Germany) DFG #AC265/1-1 (TA); IZKF Würzburg project N-304 (TA); and Dr. Werner Jackstädt Foundation (TA).

Disclosure: **J.A. Gambril**, None; **K.R. Sloan**, None; **T.A. Swain**, None; **C. Huisingh**, None; **A.V. Zarubina**, None; **J.D. Messinger**, None; **T. Ach**, None; **C.A. Curcio**, Heidelberg Engineering (F)

References

1. Yung M, Klufas MA, Sarraf D. Clinical applications of fundus autofluorescence in retinal disease. *Int J Retina Vitreous*. 2016;2:12.
2. Delori F, Greenberg JP, Woods RL, et al. Quantitative measurements of autofluorescence with the scanning laser ophthalmoscope. *Invest Ophthalmol Vis Sci*. 2011;52:9379–9390.
3. Dysli C, Wolf S, Berezin MY, Sauer L, Hammer M, Zinkernagel MS. Fluorescence lifetime imaging ophthalmoscopy. *Prog Retin Eye Res*. 2017;60:120–143.
4. Domalpally A, Clemons TE, Danis RP, et al.; Writing Committee for the Optos PEripheral RetinA Study. Peripheral retinal changes associated with age-related macular degeneration in the Age-Related Eye Disease Study 2: Age-Related Eye Disease Study 2 Report Number 12 by the Age-Related Eye Disease Study 2 Optos PEripheral RetinA (OPERA) Study Research Group. *Ophthalmology*. 2017;124:479–487.
5. Granger CE, Yang Q, Song H, et al. Human retinal pigment epithelium: in vivo cell morphometry, multispectral autofluorescence, and relationship to cone mosaic. *Invest Ophthalmol Vis Sci*. 2018;59:5705–5716.
6. Holz FG, Sadda S, Staurenghi G, et al. Imaging protocols for clinical studies in age-related macular degeneration – recommendations from Classification of Atrophy (CAM) Consensus Meeting. *Ophthalmology*. 2017;124:464–478.
7. Feeney L. Lipofuscin and melanin of human retinal pigment epithelium. Fluorescence, enzyme cytochemical and ultrastructural studies. *Invest Ophthalmol Vis Sci*. 1978;17:583–600.
8. Wing GL, Blanchard GC, Weiter JL. The topography and age relationship of lipofuscin concentration in the retinal pigment epithelium. *Invest Ophthalmol Vis Sci*. 1978;17:601–617.
9. Delori FC, Goger DG, Dorey CK. Age-related accumulation and spatial distribution of lipofuscin in RPE of normal subjects. *Invest Ophthalmol Vis Sci*. 2001;42:1855–1866.
10. Ach T, Huisingh C, McGwin G Jr, et al. Quantitative autofluorescence and cell density maps of the human retinal pigment epithelium. *Invest Ophthalmol Vis Sci*. 2014;55:4832–4841.

11. Warburton S, Davis WE, Southwick K, et al. Proteomic and phototoxic characterization of melanolipofuscin: correlation to disease and model for its origin. *Mol Vis*. 2007;13:318–329.
12. Ng KP, Gugiu B, Renganathan K, et al. Retinal pigment epithelium lipofuscin proteomics. *Mol Cell Proteomics*. 2008; 7:1397–1405.
13. Sparrow JR, Gregory-Roberts E, Yamamoto K, et al. The bisretinoids of retinal pigment epithelium. *Prog Retin Eye Res*. 2012;31:121–135.
14. Bhosale P, Serban B, Bernstein PS. Retinal carotenoids can attenuate formation of A2E in the retinal pigment epithelium. *Arch Biochem Biophys*. 2009;483:175–181.
15. Ablonczy Z, Higbee D, Anderson DM, et al. Lack of correlation between the spatial distribution of A2E and lipofuscin fluorescence in the human retinal pigment epithelium. *Invest Ophthalmol Vis Sci*. 2013;54:5535–5542.
16. Zemski Berry KA, Gordon WC, Murphy RC, Bazan NG. Spatial organization of lipids in the human retina and optic nerve by MALDI imaging mass spectrometry. *J Lipid Res*. 2014;55:504–515.
17. Adler L IV, Boyer NP, Anderson DM, et al. Determination of N-retinylidene-N-retinylethanolamine (A2E) levels in central and peripheral areas of human retinal pigment epithelium. *Photochem Photobiol Sci*. 2015;14:1983–1990.
18. Pallitto P, Ablonczy Z, Jones EE, et al. A2E and lipofuscin distributions in macaque retinal pigment epithelium are similar to human. *Photochem Photobiol Sci*. 2015;14:1888–1895.
19. Anderson DMG, Ablonczy Z, Koutalos Y, et al. Bis(monoacylglycero)phosphate lipids in the retinal pigment epithelium implicate lysosomal/endosomal dysfunction in a model of Stargardt disease and human retinas. *Sci Rep*. 2017;7:17352.
20. Kim HJ, Sparrow JR. Novel bisretinoids of human retina are lyso alkyl ether glycerophosphoethanolamine-bearing A2PE species. *J Lipid Res*. 2018;59:1620–1629.
21. Steinberg RH, Wood I, Hogan MJ. Pigment epithelial ensheathment and phagocytosis of extrafoveal cones in human retina. *Philos Trans R Soc Lond B Biol Sci*. 1977;277:459–474.
22. Feeney-Burns L, Hilderbrand E, Eldridge S. Aging human RPE: morphometric analysis of macular, equatorial, and peripheral cells. *Invest Ophthalmol Vis Sci*. 1984;25:195–200.
23. Zanzottera EC, Messinger JD, Ach T, Smith RT, Freund KB, Curcio CA. The Project MACULA retinal pigment epithelium grading system for histology and optical coherence tomography in age-related macular degeneration. *Invest Ophthalmol Vis Sci*. 2015;56:3253–3268.
24. Zanzottera EC, Messinger JD, Ach T, Smith RT, Curcio CA. Subducted and melanotic cells in advanced age-related macular degeneration are derived from retinal pigment epithelium. *Invest Ophthalmol Vis Sci*. 2015;56:3269–3278.
25. Ach T, Tolstik E, Messinger JD, Zarubina AV, Heintzmann R, Curcio CA. Lipofuscin re-distribution and loss accompanied by cytoskeletal stress in retinal pigment epithelium of eyes with age-related macular degeneration. *Invest Ophthalmol Vis Sci*. 2015;56:3242–3252.
26. Balaratnasingam C, Messinger JD, Sloan KR, Yannuzzi LA, Freund KB, Curcio CA. Histologic and optical coherence tomographic correlations in drusenoid pigment epithelium detachment in age-related macular degeneration. *Ophthalmology*. 2017;124:644–656.
27. Curcio CA, Zanzottera EC, Ach T, Balaratnasingam C, Freund KB. Activated retinal pigment epithelium, an optical coherence tomography biomarker for progression in age-related macular degeneration. *Invest Ophthalmol Vis Sci*. 2017;58: BIO211–BIO226.
28. Pollreisz A, Messinger JD, Sloan KR, et al. Visualizing melanosomes, lipofuscin, and melanolipofuscin in human retinal pigment epithelium using serial block face scanning electron microscopy. *Exp Eye Res*. 2018;166:131–139.
29. Rudolf M, Vogt SD, Curcio CA, et al. Histologic basis of variations in retinal pigment epithelium autofluorescence in eyes with geographic atrophy. *Ophthalmology*. 2013;120: 821–828.
30. Tong Y, Ben Ami T, Hong S, et al. Hyperspectral autofluorescence imaging of drusen and retinal pigment epithelium in donor eyes with age-related macular degeneration. *Retina*. 2016;36:S127–S136.
31. Sarks JP, Sarks SH, Killingsworth MC. Evolution of geographic atrophy of the retinal pigment epithelium. *Eye*. 1988;2:552–577.
32. Vogt SD, Curcio CA, Wang L, et al. Retinal pigment epithelial expression of complement regulator CD46 is altered early in the course of geographic atrophy. *Exp Eye Res*. 2011;93:413–423
33. Li M, Huisingh C, Messinger JD, et al. Histology of geographic atrophy secondary to age-related macular degeneration: a multilayer approach. *Retina*. 2018;38:1937–1953.
34. Zanzottera EC, Ach T, Huisingh C, Messinger JD, Spaide RF, Curcio CA. Visualizing retinal pigment epithelium phenotypes in the transition to geographic atrophy in age-related macular degeneration. *Retina*. 2016;36:S12–S25.
35. Klein ML, Ferris FL III, Armstrong J, et al. Retinal precursors and the development of geographic atrophy in age-related macular degeneration. *Ophthalmology*. 2008;115:1026–1031.
36. Ouyang Y, Heussen FM, Hariri A, Keane PA, Sadda SR. Optical coherence tomography-based observation of the natural history of drusenoid lesion in eyes with dry age-related macular degeneration. *Ophthalmology*. 2013;120:2656–2665.
37. Spaide RF, Yannuzzi L, Freund KB, Mullins R, Stone E. Eyes with subretinal drusenoid deposits and no drusen: progression of macular findings. *Retina*. 2019;39:12–26.
38. Chen KC, Jung JJ, Curcio CA, et al. Intraretinal hyperreflective foci in acquired vitelliform lesions of the macula: clinical and histologic study. *Am J Ophthalmol*. 2016;164:89–98.
39. Gliem M, Muller PL, Finger RP, McGuinness MB, Holz FG, Charbel Issa P. Quantitative fundus autofluorescence in early and intermediate age-related macular degeneration. *JAMA Ophthalmol*. 2016;134:817–824.
40. Orellana-Rios J, Yokoyama S, Agee JM, et al. Quantitative fundus autofluorescence in non-neovascular age-related macular degeneration. *Ophthalmic Surg Lasers Imaging Retina*. 2018;49:S34–S42.
41. Sparrow JR, Boulton M. RPE lipofuscin and its role in retinal pathobiology. *Exp Eye Res*. 2005;80:595–606.
42. Wu Z, Luu CD, Ayton LN, et al. Optical coherence tomography-defined changes preceding the development of drusen-associated atrophy in age-related macular degeneration. *Ophthalmology*. 2014;121:2415–2422.
43. Wu Z, Luu CD, Ayton LN, et al. Fundus autofluorescence characteristics of nascent geographic atrophy in age-related macular degeneration. *Invest Ophthalmol Vis Sci*. 2015;56: 1546–1552.
44. Balaratnasingam C, Yannuzzi LA, Curcio CA, et al. Associations between retinal pigment epithelium and drusen volume changes during the lifecycle of large drusenoid pigment epithelial detachments. *Invest Ophthalmol Vis Sci*. 2016;57: 5479–5489.
45. Schlanitz FG, Baumann B, Kundi M, et al. Drusen volume development over time and its relevance to the course of age-related macular degeneration. *Br J Ophthalmol*. 2016;101: 198–203.
46. Pilgrim MG, Lengyel I, Lanzirotti A, et al. Sub-retinal pigment epithelial deposition of drusen components including hydroxyapatite in a primary cell culture model. *Invest Ophthalmol Vis Sci*. 2017;58:708–719.

Investigative Ophthalmology & Visual Science

47. Schlanitz F, Baumann B, Sacu S, et al. Impact of drusen and drusenoid retinal pigment epithelium elevation size and structure on the integrity of the retinal pigment epithelium layer. *Br J Ophthalmol*. 2019;103:227–232.
48. Rossi EA, Rangel-Fonseca P, Parkins K, et al. In vivo imaging of retinal pigment epithelium cells in age related macular degeneration. *Biomed Opt Express*. 2013;4:2527–2539.
49. Morgan JI, Dubra A, Wolfe R, Merigan WH, Williams DR. In vivo autofluorescence imaging of the human and macaque retinal pigment epithelial cell mosaic. *Invest Ophthalmol Vis Sci*. 2009;50:1350–1359.
50. Mehta N, Chong J, Tsui E, et al. Presumed foveal bacillary layer detachment in a patient with toxoplasmosis chorioretinitis and pachychoroid disease [published online ahead of print]. *Retin Cases Brief Rep*. doi:10.1097/ICB.0000000000000817.
51. Green WR, Enger C. Age-related macular degeneration histopathologic studies: the 1992 Lorenz E. Zimmerman Lecture. *Ophthalmology*. 1993;100:1519–1535.
52. Curcio CA, Messinger JD, Sloan KR, McGwin G Jr, Medeiros NE, Spaide RF. Subretinal drusenoid deposits in non-neovascular age-related macular degeneration: morphology, prevalence, topography, and biogenesis model. *Retina*. 2013;33:265–276.
53. Schindelin J, Arganda-Carreras I, Frise E, et al. Fiji: an open-source platform for biological-image analysis. *Nat Methods*. 2012;9:676–682.
54. Burke JM. Epithelial phenotype and the RPE: is the answer blowing in the Wnt? *Prog Retin Eye Res*. 2008;27:579–595.
55. Anderson DH, Mullins RF, Hageman GS, Johnson LV. A role for local inflammation in the formation of drusen in the aging eye. *Am J Ophthalmol*. 2002;134:411–431.
56. Curcio CA, Balaratnasingam C, Messinger JD, Yannuzzi LA, Freund KB. Correlation of type 1 neovascularization associated with acquired vitelliform lesion in the setting of age-related macular degeneration. *Am J Ophthalmol*. 2015;160:1024–1033.
57. Futter CE. The molecular regulation of organelle transport in mammalian retinal pigment epithelial cells. *Pigment Cell Res*. 2006;19:104–111.
58. Swanson J, Bushnell A, Silverstein SC. Tubular lysosome morphology and distribution within macrophages depend on the integrity of cytoplasmic microtubules. *Proc Natl Acad Sci U S A*. 1987;84:1921–1925.
59. Swanson JA, Locke A, Ansel P, Hollenbeck PJ. Radial movement of lysosomes along microtubules in permeabilized macrophages. *J Cell Sci*. 1992;103:201–209.
60. Semenova I, Burakov A, Berardone N, et al. Actin dynamics is essential for myosin-based transport of membrane organelles. *Curr Biol*. 2008;18:1581–1586.
61. Bakker AC, Webster P, Jacob WA, Andrews NW. Homotypic fusion between aggregated lysosomes triggered by elevated [Ca2+]i in fibroblasts. *J Cell Sci*. 1997;110:2227–2238.
62. Bosch E, Horwitz J, Bok D. Phagocytosis of outer segments by retinal pigment epithelium: phagosome-lysosome interaction. *J Histochem Cytochem*. 1993;41:253–263.
63. Dunaief JL, Dentchev T, Ying GS, Milam AH. The role of apoptosis in age-related macular degeneration. *Arch Ophthalmol*. 2002;120:1435–1442.
64. Kaneko H, Dridi S, Tarallo V, et al. DICER1 deficit induces *Alu* RNA toxicity in age-related macular degeneration. *Nature*. 2011;471:325–330.
65. Kim Y, Tarallo V, Kerur N, et al. DICER1/Alu RNA dysmetabolism induces caspase-8-mediated cell death in age-related macular degeneration. *Proc Natl Acad Sci U S A*. 2014;111:16082–16087.
66. Kerr JF, Wyllie AH, Currie AR. Apoptosis: a basic biological phenomenon with wide-ranging implications in tissue kinetics. *Br J Cancer*. 1972;26:239–257.
67. Rudolf M, Clark ME, Chimento M, Li C-M, Medeiros NE, Curcio CA. Prevalence and morphology of druse types in the macula and periphery of eyes with age-related maculopathy. *Invest Ophthalmol Vis Sci*. 2008;49:1200–1209.
68. Rossberger S, Ach T, Best G, Cremer C, Heintzmann R, Dithmar S. High-resolution imaging of autofluorescent particles within drusen using structured illumination microscopy. *Br J Ophthalmol*. 2013;97:518–523.
69. Tan AC, Pilgrim M, Fearn S, et al. Calcified nodules in retinal drusen are associated with disease progression with age-related macular degeneration. *Sci Transl Med*. 2018;10:466–477.
70. Chen M, Rajapakse D, Fraczek M, Luo C, Forrester JV, Xu H. Retinal pigment epithelial cell multinucleation in the aging eye—a mechanism to repair damage and maintain homoeostasis. *Aging Cell*. 2016;15:436–445.
71. Jiang Y, Qi X, Chrenek MA, et al. Functional principal component analysis reveals discriminating categories of retinal pigment epithelial morphology in mice. *Invest Ophthalmol Vis Sci*. 2013;54:7274–7283.
72. Rashid A, Bhatia SK, Mazzitello KI, et al. RPE cell and sheet properties in normal and diseased eyes. *Adv Exp Med Biol*. 2016;854:757–763.
73. Kim SY, Yang HJ, Chang YS, et al. Deletion of aryl hydrocarbon receptor AHR in mice leads to subretinal accumulation of microglia and rpe atrophy. *Invest Ophthalmol Vis Sci*. 2014;55:6031–6040.
74. Saksens NT, Krebs MP, Schoenmaker-Koller FE, et al. Mutations in CTNNA1 cause butterfly-shaped pigment dystrophy and perturbed retinal pigment epithelium integrity. *Nat Genet*. 2016;48:144–151.
75. Monés J, Garcia M, Biarnés M, Lakkaraju A, Ferraro L. Drusen ooze: a novel hypothesis in geographic atrophy. *Ophthalmology Retina*. 2017;1:461–473.
76. Kooijman AC. Light distribution on the retina of a wide-angle theoretical eye. *J Opt Soc Am*. 1983;73:1544–1550.
77. Pflibsen KP, Pomerantzeff O, Ross RN. Retinal illuminance using a wide-angle model of the eye. *J Opt Soc Am A*. 1988;5:146–150.
78. Delcourt C, Cougnard-Gregoire A, Boniol M, et al. Lifetime exposure to ambient ultraviolet radiation and the risk for cataract extraction and age-related macular degeneration: the Alienor Study. *Invest Ophthalmol Vis Sci*. 2014;55:7619–7627.
79. Zhou H, Zhang H, Yu A, Xie J. Association between sunlight exposure and risk of age-related macular degeneration: a meta-analysis. *BMC Ophthalmol*. 2018;18:331.
80. Eldred GE, Lasky MR. Retinal age pigments generated by self-assembling lysosomotropic detergents. *Nature*. 1993;361:724–726.
81. Dorey CK, Wu G, Ebenstein D, Garsd A, Weiter JJ. Cell loss in the aging retina: relationship to lipofuscin accumulation and macular degeneration. *Invest Ophthalmol Vis Sci*. 1989;30:1691–1699.
82. Curcio CA, Millican CL, Allen KA, Kalina RE. Aging of the human photoreceptor mosaic: evidence for selective vulnerability of rods in central retina. *Invest Ophthalmol Vis Sci*. 1993;34:3278–3296.
83. Curcio CA. Antecedents of soft drusen, the specific deposit of age-related macular degeneration, in the biology of human macula. *Invest Ophthalmol Vis Sci*. 2018;59:AMD182–AMD194.
84. Mata NL, Lichter JB, Vogel R, Han Y, Bui TV, Singerman LJ. Investigation of oral fenretinide for treatment of geographic atrophy in age-related macular degeneration. *Retina*. 2013;33:498–507.
85. Rosenfeld PJ, Dugel PU, Holz FG, et al. Emixustat hydrochloride for geographic atrophy secondary to age-related macular

degeneration: a randomized clinical trial. *Ophthalmology*. 2018;125:1556–1567.

86. Jacobson SG, Cideciyan AV, Regunath G, et al. Night blindness in Sorsby's fundus dystrophy reversed by vitamin A. *Nat Genet*. 1995;11:27–32.
87. Owsley C, McGwin G Jr, Jackson GR, et al. Effect of short-term, high-dose retinol on dark adaptation in aging and early age-related maculopathy. *Invest Ophthalmol Vis Sci*. 2006;47:1310–1318.
88. Heintzmann R. Band-limit and appropriate sampling in microscopy. In: Celis JE, ed. *Cell Biology: A Laboratory Handbook*. Vol. 3. Elsevier Academic Press; 2006:29–36.
89. Grieve K, Gofas-Salas E, Ferguson RD, Sahel JA, Paques M, Rossi EA. In vivo near-infrared autofluorescence imaging of retinal pigment epithelial cells with 757 nm excitation. *Biomed Opt Express*. 2018;9:5946–5961.
90. Liu T, Jung H, Liu J, Droettboom M, Tam J. Noninvasive near infrared autofluorescence imaging of retinal pigment epithelial cells in the human retina using adaptive optics. *Biomed Opt Express*. 2017;8:4348–4360.
91. Ding JD, Johnson LV, Herrmann R, et al. Anti-amyloid therapy protects against retinal pigmented epithelium damage and vision loss in a model of age-related macular degeneration. *Proc Natl Acad Sci U S A*. 2011;108:E279–E287.
92. Starnes AC, Huisingh C, McGwin G, et al. Multi-nucleate retinal pigment epithelium cells of the human macula exhibit a characteristic and highly specific distribution. *Vis Neurosci*. 2016;33:E001.
93. Paavo M, Lee W, Merriam J, et al. Intraretinal correlates of reticular pseudodrusen revealed by autofluorescence and en face OCT. *Invest Ophthalmol Vis Sci*. 2017;58:4769–4777.
94. Krebs W, Krebs I. *Primate Retina and Choroid: Atlas of Fine Structure in Man and Monkey*. New York: Springer Verlag; 1991.

Investigative Ophthalmology & Visual Science